HDR Denoising and Deblurring by Learning Spatio-temporal Distortion Models

Uğur Çoğalan[1]   Mojtaba Bemana[1]   Karol Myszkowski[1]   Hans-Peter Seidel[1]   Tobias Ritschel[2]

[1]MPI Informatik   [2]University College London

Abstract

We seek to reconstruct sharp and noise-free high-dynamic range (HDR) video from a dual-exposure sensor that records different low-dynamic range (LDR) information in different pixel columns: Odd columns provide low-exposure, sharp, but noisy information; even columns complement this with less noisy, high-exposure, but motion-blurred data. Previous LDR work learns to deblur and denoise (DISTORTED→CLEAN) supervised by pairs of CLEAN and DISTORTED images. Regrettably, capturing DISTORTED sensor readings is time-consuming; as well, there is a lack of CLEAN HDR videos. We suggest a method to overcome those two limitations. First, we learn a different function instead: CLEAN→DISTORTED, which generates samples containing correlated pixel noise, and row and column noise, as well as motion blur from a low number of CLEAN sensor readings. Second, as there is not enough CLEAN HDR video available, we devise a method to learn from LDR video instead. Our approach compares favorably to several strong baselines, and can boost existing methods when they are re-trained on our data. Combined with spatial and temporal super-resolution, it enables applications such as re-lighting.

1. Introduction

Common cameras only capture a limited range of luminance values (LDR), while many display and editing tasks would greatly benefit from capturing a higher range of luminance values (HDR) [83]. Modern sensors, such as some CMOSIS CMV and Sony IMX sensors, allow one to configure different levels of exposure for different spatial patterns [18, 36]. This allows HDR by spatial interleaving of different exposures across the sensor. The challenge is to combine different exposures into a coherent natural image (Fig. 1).

Let us consider, without loss of generality, a case where every even row column is captured with a low exposure and every odd row column with a high exposure. This leads to three specific distortions: First, *pixel noise* inside the image does not follow a single model anymore, but is now strongly
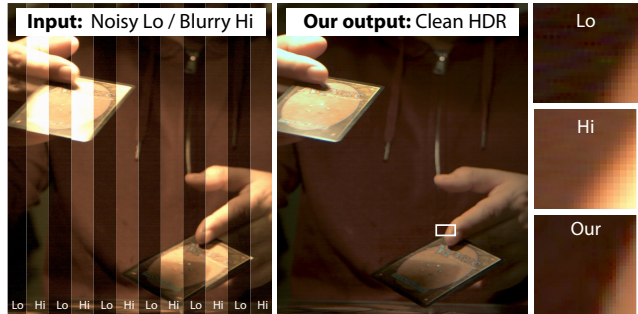

Figure 1. Our method maps low-exposure LDR data with noise and high-exposure LDR data with blur into a clean HDR image.

correlated with the column. Different exposures lead to different noise, one of the reasons why different exposures are being used in the first place: the low exposures have high noise, but are not clamped, while the high exposures have less noise but suffer from clamping. Second, such cameras suffer from increased levels of *row/column noise*, so orthogonal to the exposure layout, entire rows/columns of pixels change coherently, and differently for different exposures. Third, and most different from other sensors, the different exposure level also leads to different forms of *motion blur* (MB). Not only does MB lead to spatially varying blur, but this blur rapidly alternates between odd and even columns. Low exposures have low MB, while high exposures suffer from strong MB. In summary, these distortions do not follow any common noise or motion blur model, and hence no method making such assumptions is applicable to HDR from dual exposure.

Removing image distortions (deblurring and denoising) is now typically solved [111, 64, 73, 97] by learning a deep neural network (NN) such as a convolutional neural network (CNN) to implement DISTORTED→CLEAN. In our case, this is difficult, as capturing DISTORTED sensor readings is time-consuming, and there is also a lack of CLEAN HDR videos. We suggest a method to overcome both limitations.

Addressing the first, we learn a different function instead: CLEAN→DISTORTED, which generates samples containing correlated pixel noise, row and column noise, as well as motion blur from CLEAN sensor readings. Previous work has

1

made simplifying assumptions, such as Gaussian or Poisson noise, none of which apply to our problem. We suggest a non-parametric noise model that is expressive, yet can be trained on a low number of CLEAN-DISTORTED pairs.

Second, as there are not enough CLEAN samples which require HDR video, we supervise from LDR video instead. Unfortunately, this LDR video does not have the same type of MB as found in HDR sensor readings. Hence, we use high-speed LDR video to simulate column-alternating MB.

Our evaluation shows that this synthetic training data drives our network, resulting in state-of-the-art HDR images, but can also boost existing methods, including vanilla non-learned denoisers like BM3D, when re-tuned. Applications span different exposure ratios, where we show re-lighting in a VR/AR context as a typical HDR application.

2. Previous work

In this section, we discuss previous approaches to single (Sec. 2.1), multiple (Sec. 2.2), and in particular HDR (Sec. 2.3) image denoising and deblurring.

2.1. Single-image denoising and deblurring

Noise modeling Classic solutions involve fitting Gaussian and Poisson [34, 59] or more involved [79] distributions, sometimes under extreme conditions [11], to many pairs of CLEAN and DISTORTED images. While parametric noise models routinely are used as mathematically tractable priors, we use more expressive non-parametric models, as all we need is to generate distorted training data.

Denoising Denoising has traditionally been performed directly on noisy images using state-of-the-art algorithms such as BM3D [19], non-local means [7], and Nuclear Norms [29]. Most deep denoisers [11, 111, 110, 8, 64, 12, 30, 54, 38] are simply trained on pairs of noisy and clean images, while some work is trained without pairs [99, 55, 49, 53, 50, 6, 82, 70, 106], using GANs [13] or self-supervision [105]. The usefulness of neural networks in denoising for real sensors has been disputed [79, 11].

Blur modeling Video obtained with a high-speed camera [94, 73, 72] or beam splitters [115] enables motion blur synthesis for the purpose of generating training data using gyroscope-acquired [71] or random [68] motion.

Deblurring Non-blind deconvolution methods [118, 88, 96, 87, 108, 15, 102] restore sharp images given the blur kernel. Blind deconvolution methods attempt to derive the kernel based on various priors on either the sharp latent image or the blur kernel [23, 57, 107, 67, 25, 95, 9]. Explicit kernel derivation can be avoided in end-to-end training, where the sharp image is derived directly [73, 97], by self-supervision [60] or adversarial training [51, 52]. Video deblurring additionally capitalizes on inter-frame relationships, while assur-

ing temporal coherence of the result [46, 47, 116, 115, 94]. Deblurring can be combined either with spatial [112] or temporal [81, 41, 40] super-resolution, as done in our approach. The presence of noise, clamping and multiple exposure as in our condition adds a further challenge. Methods such as Pan et al. [78] model general distortions using CycleGAN [117], but have not been demonstrated to perform denoising.

2.2. Multi-image denoising and deblurring

A number of solutions have been proposed to capture multiple images of the same content to provide more information for ill-posed deblurring and denoising.

Fixed-exposure burst photography Burst photography combines a handful of low-exposure frames into a high-quality LDR result using efficient hand-crafted solutions deployed in cellphones [61, 32, 58, 58] or based on learning of recurrent architectures [103], or unordered sets [3], or per-pixel filter kernels [68]. The problem of read noise that accumulates from each contributing frame can be avoided in quanta burst photography that employs binary single-photon cameras to capture high-speed sequences [62].

Low/high exposure image pairs Short-exposure images are sharp but noisy, while long-exposure images are blurry but free of noise. Such *exposure pairs* have been used for non-uniform kernel deblurring [109, 102]. Along a similar line, Mustaniemi et al. [71] and Chang et al. [10] jointly learn how to denoise and deblur exposure pairs supervised by synthetic training data. Different from our goal, they produce LDR output, while we aim for HDR.

2.3. HDR images and video

HDR means covering a large range of luminance via software expansion, multiple exposure, or special sensors.

Dynamic range expansion LDR can be expanded to HDR in software. Although immense progress has been made based on CNNs [65, 22, 21], results do not yet match the quality of multi-exposure techniques or dedicated sensors.

Multi-shot A typical sensor can capture a wide range of luminances, just not within one shot. Alternatively, an *exposure sequence*, i. e., time-sequential capture of one scene at different exposure settings, can be merged into one image [63, 69, 20, 85, 26]. Further, exposure sequences can be fused into a high-quality LDR image [66, 80, 71]. When dealing with video [45, 44, 27] or when using neural networks [42, 43, 104], alignment becomes a challenge.

Single-shot Capturing exposure sequences takes time and their alignment is challenging, in particular for video. This can be alleviated by single-shot solutions relying on custom optics and sensors. Logarithmic response does not require any exposure control [91], but remains prone to noise in dark regions. Spatially-varying exposure (SVE) techniques

place a fixed [76, 90, 89, 92, 2] or adaptive [74, 75] mask of variable optical density in front of the sensor, but face problems with resolution and aliasing. Beam splitting preserves resolution with different exposures [98, 1, 48] but requires involved optics. Dual-ISO sensors, e. g., Gpixel GMAX and some of the Canon EON sensors, enable varying analogue signal gain for odd and even scanlines. Their key advantage is that variable blur between scanlines is avoided, as the exposition is fixed for the whole sensor. On the other hand, instead of collecting more photons in the long exposure and reducing noise this way, only a noisy short exposure is taken, and the long exposure is emulated by increasing ISO, which leads to further noise amplification. Therefore, denoising and deinterlacing are the key challenges for processing dual-ISO frames [31, 24], including data-driven solutions such as learned artifact dictionaries [16] and CNNs [119]. Dual-gain sensors in high-end Canon and professional cinematographic Alexa (ARRI) cameras employ a similar idea but generate two full frames with different analog gains to improve the ratio of read noise to the signal in the high-gain image. The problem of noise inherent to short exposures, needed to avoid highlight clipping, is reduced by large photosites.

Dual-exposure CMOS sensors enable varying exposures for odd and even scanlines (some Aptina AR and Sony IMX sensors [36]) or columns (CMOSIS CMV12000 [18]). Gu et al. [28] perform flow-compensated interpolation for subimage deinterlacing so that differently exposed, full-resolution images are obtained. Cho et al. [14] directly calibrate scanlines using bilateral filters followed by motion blur removal [56] and sharpening. Along similar lines, Heide et al. [35] propose an end-to-end optimization, which jointly accounts for demosaicking, deinterlacing, denoising, and deconvolution. An and Lee [4] restore under- and over-exposed pixels using a CNN, but no results for real sensor data are demonstrated. Our work performs joint denoising, deinterlacing and deblurring, trained on a small set of captured data, resulting in high-quality HDR.

Exposure on modern sensors To better understand the trade-off between single- and dual-exposure sensors, we first conducted a pilot experiment to evaluate the exposure-dependent noise for three different kinds of sensors: iPhone (Apple iPhone 8), Canon (Canon EOS 550D) and Axiom-beta (CMOSIS CMV12000; a full-frame single-exposure setup). For each sensor 600 images of the same scene has been captured in low- and high-exposure (four time longer) modes. An iPhone records 14, Canon and Axiom-beta 12 bits. All readings were converted to floating point values between 0 and 4. High exposure was divided by four to match the same range. For low exposure, an ideal (as the scene is static) burst fusion was simulated by averaging random four-tuples. The average of all low-exposure frames is considered the reference for each sensor. Note, that by construction the reference of the high and low mode is the
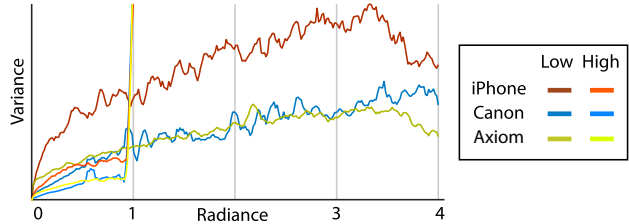

Figure 2. Noise for contemporary sensors at different exposures and intensity: The horizontal axis is unit radiance. The vertical axis is variance (less is better). Different hues depict different sensors. Bright colors are high, dark colors are low exposure.
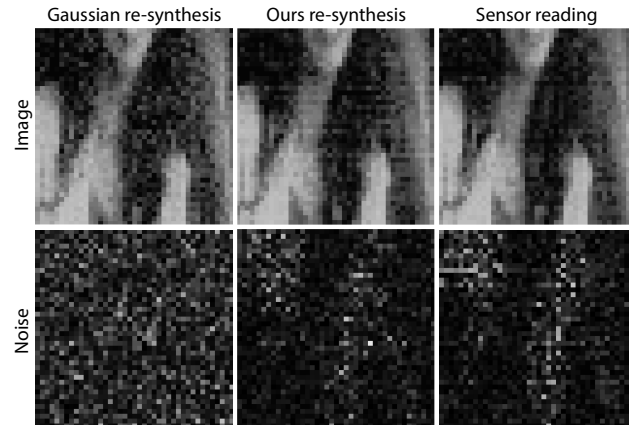

Figure 3. A Gaussian noise model **(left)**, our low-exposure re-synthesis **(middle)** from a noise-free high-exposure reference (not shown), and a real low-exposure sensor reading reference **(right)**. Note the long-range correlation across ours and the reference.

same. Then, for every quantized (12 or 14 bit) value L of the reference of each sensor, we select one pixel with that value and compute the variance $\mathrm{Var}(L)$ of all readings in all images. A high value means that particular sensor for this mode and this absolute radiance has more noise (worse).

Fig. 2 shows that for all sensors, as expected, noise increases with signal [26, 37]. We further see, that around 0.25 the variance for high exposure diverges (clipping), indicating that these or even higher values cannot be used with long exposure. More importantly, we also see that low exposure has a higher variance until the point where the high exposure clips. This trend is true for all sensors, so between 0 and 1: every sensor (hue) at its low exposure mode (brightness) has a higher variance than the high exposure. This can be attributed to read noise of each burst frame that is accumulated [62]. This indicates that combining low exposures, even under the ideal condition of no motion, is no immediate solution. In summary, no single strategy of either averaging low exposures or just using one high exposure is successful across the entire HDR range. We conclude, that there is a benefit of sensors, which have access to different exposure at different spatial locations.
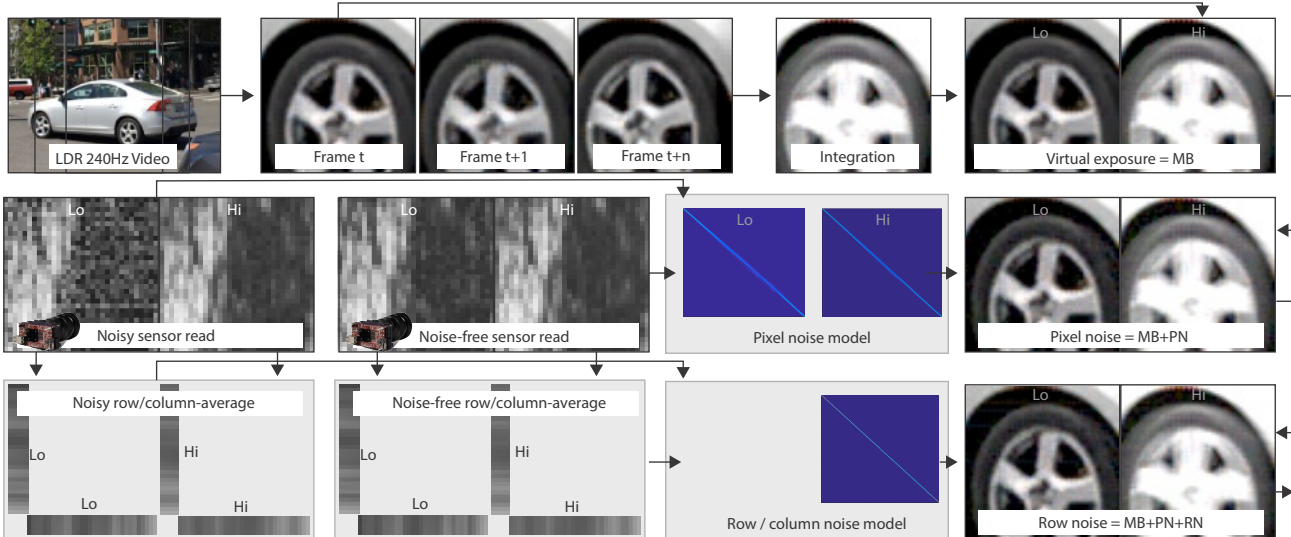
Figure 4. Our proposed HDR distortion generation pipeline: We start from LDR 240 Hz video in the top left, from which frames t to $t+n$ are extracted, integrated, and virtually exposed to produce an image with MB (**first row**). Next, we take pairs of noisy and time-averaged noise-free sensor readings, and produce a non-parametric noise mode (histogram) for low and high exposure. This noise model is added to the virtual exposure image MB (**second row**). Finally, a model of row and column noise is extracted by averaging vertically or horizontally; this can be added to the pixel noise image, producing the final image with all distortions present (**third row**).

3. HDR exposure distortion and back

Our approach has two steps: learning a model to synthesize distortions to train on (Sec. 3.1; an example result in Fig. 3) and learning to remove distortions (Sec. 3.2).

3.1. Clean-to-distorted

There are three distortion steps we describe in the order of the underlying physics (Fig. 4): motion blur (Sec. 3.1.1), pixel noise (Sec. 3.1.2), and row/column noise (Sec. 3.1.3). For all steps, we will look at the analysis from noisy sensor readings to devise a statistical model for inference from DISTORTED, and a synthesis step to apply it to CLEAN.

3.1.1 Motion blur

With different exposures in different columns, their MB is also different. For example, at exposure ratio $r = 4$, MB also is four times longer and the image is a mix of sharp and blurry columns. As getting reference data without MB, in particular HDR, is difficult, we turn to existing LDR high-speed video footage to simulate multi-exposure MB.

Data We use 123 videos from the Adobe High-speed Video Dataset [94] which have no, or negligible, inherent MB in a total of 8000 frames. Note that these are not captured with our sensor, and are LDR. They are neither input to nor output from of our approach and only provide supervision.

Synthesis Synthesis starts from a random frame of 8-bit LDR high-speed video I_{LDR}. It is converted to floating

point, and an inverse gamma is applied at $\gamma = 2.2$. We call this the *low frame* image, denoted $I_{\mathrm{L}} = I_{\mathrm{LDR}}^{\gamma}$. Since our sensor assures that the low and high exposures are ending at the same time [18], to simulate the high frame exposure we average four subsequent I_{L}, then scale by the exposure ratio, and clamp as in

$$I_{\mathrm{H}} = \mathtt{clamp}(r \times \mathbb{E}_{t \in \{0,1,2,3\}}[I_{\mathrm{L}}(t)]).$$

Finally, the low-frame pixels are inserted into the even columns and the high frames into the odd ones, resulting in the motion-blurred image I_{MB}.

3.1.2 Pixel noise

Pixel noise, which occurs in the sensor, is applied after motion blur, which happens in the optics. Instead of employing a parametric noise model that has the strengths as priors and for analysis, we use non-parametric histograms to capture a noise model well-suited for generation. Prior to the noise model derivation, we remove the fixed pattern noise [37].

Data We assume we have a limited amount of GT sensor readings available. In practice, we use no more than 30 pairs of images (not video) captured with the target sensor of everyday scenes, as well as a ground truth acquired by averaging the result of 100 captures of the scene at a very low exposure (so as to make clipping effects negligible) and using a very long exposure.

Analysis The noise is different for different exposures and also for different color channels. We build a model $p_{c,e}(x|y)$,

the probability that when the GT value is y, the sensor will read x for channel c and exposure e. A separate model is maintained for every channel in every exposure, leading to six models for three color channels and two exposures. While we notice the noise models to be similar for different channels at the same exposure, it is, unsurprisingly, different for different exposure. Histograms $H_{c,e}[x][y]$ are used to represent the probability distribution over x for each y in channel c at exposure e. To construct all histograms, every pair of sensor readings and its ground truth, as well as every pixel and every channel, are iterated, and bin x for histogram y is incremented when the GT pixel is y and the sensor reading is x for channel c and exposure e. The number of histogram bins depends on the bit depth, typically 12 bits, resulting in 4096 bins. After analysis, all histograms are converted into inverse cumulative histograms $C_{c,e}[x][y]$, allowing us to sample from them in constant time.

Synthesis Noise synthesis is applied to I_{MB}, the image with simulated MB. Every pixel and every channel of the MB image I_{MB} is iterated to obtain a GT value y. A random number $\xi_{c,e}$ is used to look up the respective cumulative histogram $C_{c,e}$ to produce a simulated sensor value x. Combining all pixels, channels and exposures results in a virtual synthetic image I_{PN} involving MB and pixel noise.

3.1.3 Row/column noise

At short exposures more structured forms of noise can become important, one of them being *row/column* noise. This is not to be mistaken with fixed-pattern noise that frequently is spatially-correlated, but much easier to correct. In row/column noise, pixels do not change independently; rather, all pixels in a row/column change in correlation, i. e., the entire row/column is darkened or brightened. This is because in the CMOSIS CMV12000 (global shutter) sensor pixel read-out is performed sequentially row-by-row, resulting in differences between the rows. The analog pixel values are then passed to a column gain amplifier and a column analog-digital converter (ADC), which are used to speed up processing, but introduce differences between the columns [18]. As those effects are visually distracting, we synthesize and ultimately remove them.

Analysis We again iterate all pairs of GT and sensor images, but instead of working on pixels, we now work on entire rows/columns. In particular we look at the six separate means across every row/column for every channel and exposure. We denote this mean as $\bar{x}$ in the sensor image and as $\bar{y}$ in the GT image. We now proceed as with pixel noise and build a model in the form of a histogram, resulting in the inverse cumulative row/column noise model $\bar{C}_{c,e}[\bar{x}][\bar{y}]$.

Synthesis Synthesis of row/column noise starts from the image with synthetic MB and pixel noise I_{PN}. We iterate

every row, channel and exposure, compute the row/column mean $\bar{y}_{c,e}$ and again use a random number $\bar{\xi}_{c,e}$ to draw from $\bar{C}_{c,e}[\bar{\xi}][\bar{y}]$. To make the row/column mean match the desired mean, we add the difference of the means to the row/column, resulting in the final synthetic noisy image I_{All}.

3.2. Distorted-to-clean

We use a U-Net [86] with residual connections [33] and sub-pixel convolutions [93] to map distorted $128 \times 64 \times 8$ patches to $128 \times 128 \times 8$ clean patches under an SSIM loss [114] in linear space. Output is converted to RGB and gamma-corrected after the loss.

4. Results

We present quantitative and qualitative evaluation on deblurring/denoising (Sec. 4.1), super-resolution (Sec. 4.2), and HDR illumination reconstruction (Sec. 4.3) tasks. Interactive comparison and videos can be found at https://deephdr.mpi-inf.mpg.de.

All test images have been captured using an Axiom-beta camera with a CMOSIS CMV12000 sensor [18] and a Canon EFS 18-135 mm lens at resolution 4096×3072 RAW 12-bit pixels, using the lowest gain with exposure ratio 4 (or 16 when explicitly mentioned) and (low) exposure time varying from 1 to 8 ms. Although our noise model is created for a given fixed ratio, the exposure times for the two discrete exposures can vary continuously as we show in the supplemental materials. All results are shown after gamma correction and photographic tone mapping [84]. CMOSIS CMV12000 sensor [18] is a CMOS sensor that features global shutter, large pixel sizes, low dark current noise, and is relatively inexpensive in comparison with CCD sensors with similar performance. Therefore the sensor is suitable for demanding computer vision applications and it is offered by many well-known industrial camera makers [5, 77, 100].

4.1. Denoising/deblur evaluation

We now evaluate the combination of our method and our synthetic training data as well as other ways to obtain training data and other methods for denoising and deblurring.

Methods We consider eight methods (color-coded; "Method" in Tbl. 1): Direct is a non-learned direct, physics-based fusion of the low and high frame, with bicubic upsampling [20]. Next, BM3D [19] is a gold-standard, non-deep denoiser. When BM3D is "trained" this means performing a grid search on the training data in order to find the standard deviation parameter with the the optimal DSSIM. FFDNet [111] is a state-of-the-art deep denoiser. DBGAN [52] and SRNDB [97] are recent deblurring approaches. LSD [71] is a deep multi-exposure method that produces denoised and deblurred LDR images. The final
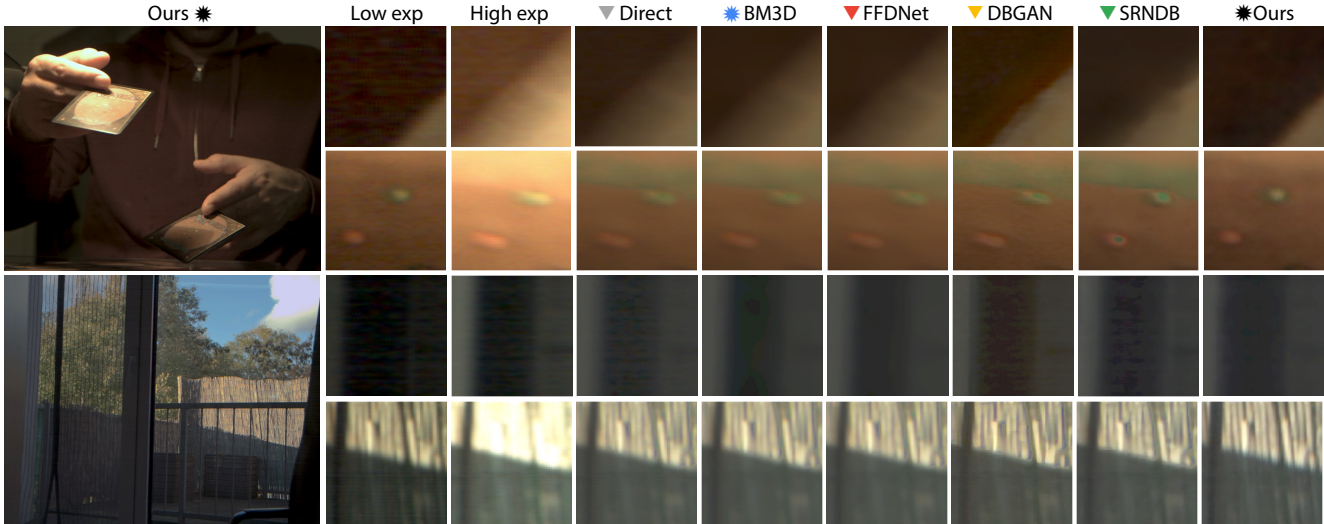
Figure 5. Comparison of different methods **(columns)** on two scenes **(rows)**. Please see the text for discussion.

method is Heide [35] which is a general image reconstruction method, capable of working with multiplexed exposures.

Training data For each method, we study how it performs when trained with different data ("Train. data" in Tbl. 1). Each type of training data has a different symbol. We denote it as "Theirs" (▼) if the authors provide a pre-trained version. "Sensor" (▲) means training on the image for which we have paired training data available directly, i. e., without our proposed re-synthesis. Please note that this training is not applicable to tasks that involve removing MB, as the supervision inevitably contains MB. Next, we study heteroscedastic Gaussian noise, "HetGau" (●) which refers to taking our training data, fitting a linear model of Gaussian parameters of the error distribution and then re-synthesizing training. Finally, we study four ablations of our training data generation: only motion blur ("OurMB", ✳), only pixel noise ("OurPN", ★), only row noise ("OurRN", ✦), and finally ("OurAll", ✳) in Tbl. 1.

Metrics We measure DSSIM [101], where less is better.

Tasks We study four tasks (four last columns in Tbl. 1): First, we remove noise in the low exposure only (Lo2Lo). Second, we remove noise and MB in the high exposure only (Hi2Hi-MB). Third, is a task where input is both exposures and output is an HDR image without noise, LoHi2HDR. The fourth task consumes low and high exposures, and removes both noise and MB to output HDR (LoHi2HDR-MB). In all tasks, the exposure ratio, 1:4, is in favor of competitors conceived for LDR use. The test set for all tasks contains 10 images.

Discussion Results are shown in Tbl. 1. Our method trained on our synthetic training data (✳) performs best on all tasks. Our ablations (✦, ★ and ✳) all perform worse than the

Table 1. Performance of different methods and different training data *(rows)* for different tasks *(columns)*. Different icon shapes denote different training; colors map to different methods.

		Task			
In Lo		✓	✗	✓	✓
In Hi+MB		✗	✓	✓	✓
Out MB		✗	✗	✓	✗
Out HDR		✗	✗	✓	✓
Train. data	Method	Error (DSSIM$\times 10^{-2}$)			
▼ Theirs	Direct [20]	7.87	7.08	3.70	5.52
▼ Theirs	BM3D [19]	2.98	4.10	2.00	2.63
▲ Sensor		2.84	——	1.90	——
● HetGau		2.75	3.86	1.76	2.32
✳ OurAll		**2.72**	3.93	1.80	2.35
▼ Theirs	FFDNet [111]	3.79	4.31	2.18	2.83
▲ Sensor		2.78	——	2.03	——
✳ OurAll		2.78	3.92	2.03	2.54
▼ Theirs	DBGAN [52]	5.31	4.88	2.95	3.32
▼ Theirs	SRN-DB [97]	3.28	4.36	2.27	2.60
▼ Theirs	LSD$_2$ [71]	——	2.94	3.24	2.46
▼ Theirs	Heide et al. [35]	5.27			
▲ Sensor	Ours	6.51	——	4.62	——
● HetGau		3.14	3.17	2.35	2.15
✦ OurRN		5.33	5.24	4.41	4.32
★ OurPN		4.24	4.60	3.01	3.06
✳ OurMB		4.23	3.63	2.17	3.15
✳ OurAll		2.75	**2.64**	**1.68**	**1.84**

Figure 6. Comparison of our reconstruction at an exposure rate of 16:1 and the best single exposure result **(inset stripes)**.

blur are visually important, and no method, including ours, can reduce one of them enough to make the other irrelevant. In summary, using the right training data helps our methods and others to solve multiple aspects of multiple tasks.

The quantitative results from above are complemented by the qualitative ones in Fig. 5. The first row shows our (✴) complete image. The second and third row show selected patches from the the low and high input, which suffer from noise or blur respectively. Directly (▼) fusing both into HDR, as in the fourth column, reduces noise and blur, but cannot remove them. The BM3D (✴) and FFDNet (▼) columns show that individual frames can be denoised, but blur remains. This is most visible in moving parts, such as the dots in the second row. Using de-blurring, as in DBGAN (▼) or SRNDB (▼), can reduce blur, but this often leads to ringing. Our joint method (✴) performs best on these.

full method, indicating all additions are relevant. Looking into how other methods trained on data synthesized using our distortion model perform (✴ and ✴), we see that first, they all improve in comparison to being trained on their original data (▼, ▼, ▼, ▼ and ▼, respectively), but, second, none can compete with our method trained on that data (✴). Only ✴, as a competing method, when tuned on our data, can compete on its home ground, Lo2Lo. We also tried training our network with other data, such as using sensor data directly (▲), hetroscedatic Gaussian noise (●), but none of these was able to capture the combination of motion blur, pixel noise and row/column noise, resulting in larger errors. As a sanity check, we also tuned BM3D on sensor data (▲) and hetroscedatic Gaussian noise (●), but no choice of parameters, even with that information, can get BM3D to perform much better on test data. A further test is to compare to ▼, which is not learned or doing anything except up-sampling and fusion; this should be a lower bound for any method or task. Finally, our approach compares favorably to Heide et al. [35] (▼), a general, powerful and flexible imaging framework that can work on multi-exposure images. When looking at performance for different tasks, we find that for simpler tasks, such as Lo2Lo, i.e., a direct denoising, unsurprisingly, our best result (✴) performs comparably to the gold standard (▼), in particular when tuned on our data (✴). When the task gets more involved, i.e., removing MB or producing HDR, the methods start to perform more similarly, but ours tends to win by a larger margin. For completeness, our analysis includes methods designed for denoising being applied to a deblurring task or vice versa. As all tasks except Lo2Lo involve components of both deblurring and denoising, we report those numbers to certify that no method solving only one of the tasks, does it so well that the DSSIM is reduced more than another method trying to solve both tasks. This is probably because both noise and
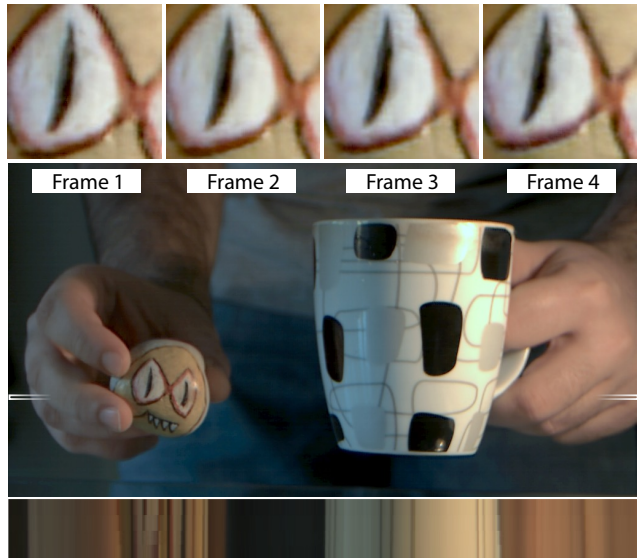

Figure 7. Four frames cropped **(top)** from an HDR video with temporal super-resolution using Oᴜʀ approach. The full frame 2 **(middle)**. An epipolar slice for the marked row **(bottom)**.
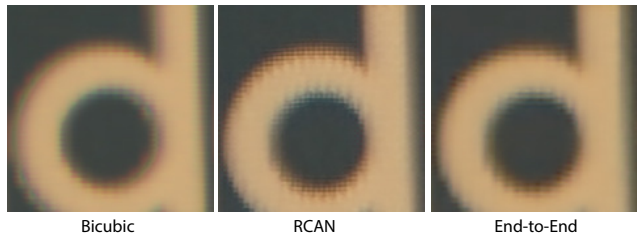

Figure 8. Spatial super-resolution.

Fig. 6 compares our result at an exposure rate of 16:1 to the best single-exposure result. We note our approach reproduces details in the bright (outdoor) part as well as in the dark (indoor) part despite the massive contrast. The best LDR fit can resolve some of the outdoor elements, but has
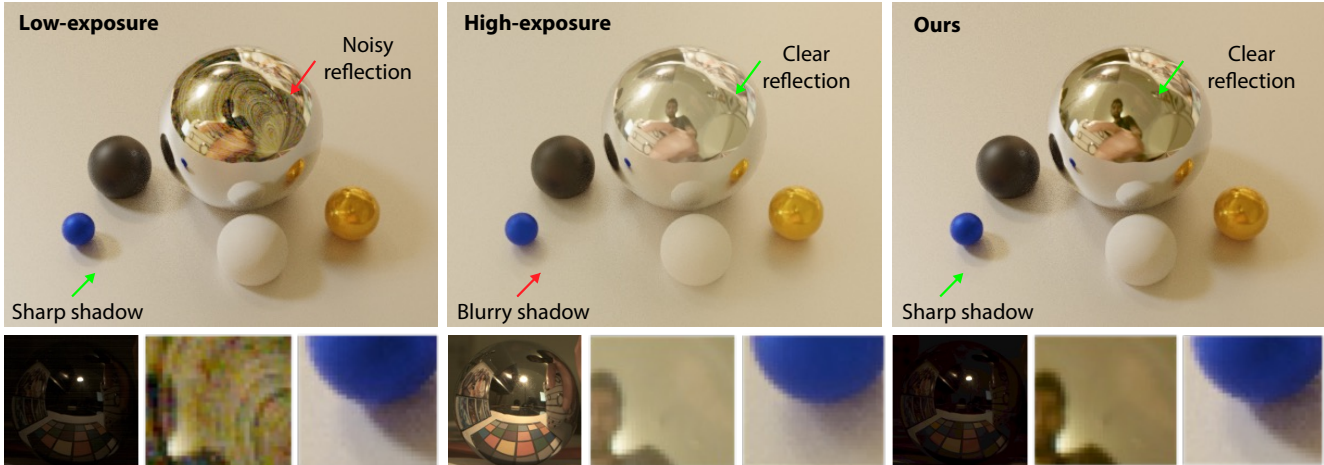
Figure 9. Rendering from a spherical illumination map captured at a low exposure (**left**), a high exposure (**middle**) and using our approach (**right**). For each approach the illumination is seen as an inset on the left. For the low exposure, the shadows are sharp, as the light source did not saturate, but the dark regions are clipped and massively noisy. For the high exposure, the dark regions are reproduced, slightly noisy, but the light source is clamped, leading to a loss in dynamic range and a loss of sharp shadows. Our method reproduces both. Note that visible overall brightness differences are expected, as clamping is present in some images, which does not conserve energy.

Table 2. HDR super-resolution in combination with denoising and deblurring. "Us-Them" means to first run `Our` non-super-resolution method, followed by: temporal [39], or spatial [113] super-resolution method. "End-to-End" means `Our` full method.

	Us-Them	End-to-End
Temporal	0.032	0.026
Spatial	0.043	0.035

no details except quantization noise in the dark part.

4.2. Temporal and spatial super-resolution

In temporal super-resolution [39], we extend the LOHI2HDR-MB task to output not a single image, but n images instead. To generate training data, we still extract sequences of n high-speed video frames, and we still call the first frame the low frame and the integral of all n frames the high exposure. The architecture is identical, except that it produces n images in the last layer. Note that the input is still only two interleaving exposures, where one has severe MB and the other severe noise. Fig. 7 shows `Our` End-to-End reconstruction, and in the supplemental materials we demonstrate a continuous adjustment of blur magnitude.

Analogously to temporal super-resolution, we can also look at spatial super-resolution [113]. Here, training data is spatially down-scaled before being used to simulate Hi and Lo frames. At training time, the decoder branch is simply repeated several times to produce output patches larger than the input patches. Fig. 8 compares a bicubic upsampling and RCAN [113] to `Our` End-to-End method.

Tbl. 2 compares our methods with [39] and [113].

4.3. Application: HDR illumination reconstruction

A key application of HDR is to use it for illumination [20]. We captured a mirror ball, removed motion blur and noise using our full method (✳), and re-rendered it using Blender's [17] path tracer with 512 samples and automatic tone and gamma mapping. The resulting image is seen in Fig. 9. We find that the non-linear mapping of MC rendering amplifies structures and noise gets more visible, in particular row noise. Using only the high exposure removes noise, but cannot capture the dynamic range, resulting in washed-out shadows. Our method succeeds in removing it, in particular row noise, resulting in sharp shadows as well as noise-free reflections. Note that some noise is present in all images due to finite MC sample count (all images computed 20 min.). The noise appears less in the high exposure, as reduced contrast results in an easier light simulation problem that leads to an overall incorrect, strongly biased solution.

5. Conclusion

We presented a CNN solution for HDR image reconstruction tailored for a single-shot dual-exposure sensor. By joint processing of low and high exposures and taking advantage of their perfect spatial and temporal registration, our solution solves a number of serious problems inherent to such sensors such as correlated noise and spatially varying blur, as well as interlacing and spatial resolution reduction. We demonstrate that, by capturing a limited amount of data specific for such sensors and using simple histograms to represent the noise statistics, we were able to generate synthetic training data that led to a better denoising and deblurring quality than achieved by existing state-of-the-art techniques. Moreover,

we show that by using our limited sensor-specific data, the performance of other techniques can greatly be improved. This is for two reasons: First, previous methods did not have access to massive amounts of training data for dual-exposure sensors, a problem we solve here by proposing the first dedicated distortion model allowing to synthesize training data. Second, dual-exposure sensors in combination with proper CNN-based denoising and deblurring provide us with much richer data managed to fuse.

References

[1] M. Aggarwal and N. Ahuja. Split aperture imaging for high dynamic range. In *ICCV*, volume 2, pages 10–17, 2001. 3

[2] C. Aguerrebere, A. Almansa, Y. Gousseau, J. Delon, and P. Musé. Single shot high dynamic range imaging using piecewise linear estimators. In *ICCP*, pages 1–10, 2014. 3

[3] Miika Aittala and Fredo Durand. Burst image deblurring using permutation invariant convolutional neural networks. In *ECCV*, 2018. 2

[4] V. G. An and C. Lee. Single-shot high dynamic range imaging via deep convolutional neural network. In *APSIPA*, pages 1768–1772, 2017. 3

[5] Basler. https://www.baslerweb.com/en/products/cameras/area-scan-cameras/basler-beat/bea400-2kc/, accessed on Mar. 15, 2021. 5

[6] Joshua Batson and Loic Royer. Noise2self: Blind denoising by self-supervision. In *ICML*, pages 524–533, 2019. 2

[7] Antoni Buades, Bartomeu Coll, and J-M Morel. A non-local algorithm for image denoising. In *CVPR*, volume 2, pages 60–65, 2005. 2

[8] Harold C Burger, Christian J Schuler, and Stefan Harmeling. Image denoising: Can plain neural networks compete with BM3D? In *CVPR*, pages 2392–2399, 2012. 2

[9] Ayan Chakrabarti. A neural approach to blind motion deblurring. In *ECCV*, pages 221–235, 2016. 2

[10] Meng Chang, Huajun Feng, Zhihai Xu, and Qi Li. Low-light image restoration with short- and long-exposure raw pairs, 2020. 2

[11] C. Chen, Q. Chen, J. Xu, and V. Koltun. Learning to see in the dark. In *CVPR*, pages 3291–3300, 2018. 2

[12] Jingwen Chen, Jiawei Chen, Hongyang Chao, and Ming Yang. Image blind denoising with generative adversarial network based noise modeling. In *CVPR*, 2018. 2

[13] Jingwen Chen, Jiawei Chen, Hongyang Chao, and Ming Yang. Image blind denoising with generative adversarial network based noise modeling. In *CVPR*, pages 3155–3164, 2018. 2

[14] Hojin Cho, Seon Joo Kim, and Seungyong Lee. Single-shot high dynamic range imaging using coded electronic shutter. *Comp. Graph. Forum*, 33(7):329–338, 2014. 3

[15] S. Cho, Jue Wang, and S. Lee. Handling outliers in non-blind image deconvolution. In *CVPR*, pages 495–502, 2011. 2

[16] Inchang Choi, Seung-Hwan Baek, and M. Kim. Reconstructing interlaced high-dynamic-range video using joint learning. *IEEE TIP*, 26:5353–5366, 2017. 3

[17] Blender Online Community. *Blender*, 2020. 8

[18] CMOSIS CMV. https://ams.com/cmv12000, accessed on Nov. 12, 2020. 1, 3, 4, 5

[19] K. Dabov, A. Foi, V. Katkovnik, and K. Egiazarian. Image denoising by sparse 3-D transform-domain collaborative filtering. *IEEE TIP*, 16(8):2080–2095, 2007. 2, 5, 6

[20] Paul E. Debevec and Jitendra Malik. Recovering high dynamic range radiance maps from photographs. In *Proc. SIGGRAPH*, page 369–378, 1997. 2, 5, 6, 8

[21] Gabriel Eilertsen, Joel Kronander, Gyorgy Denes, Rafał K. Mantiuk, and Jonas Unger. HDR image reconstruction from a single exposure using deep CNNs. *ACM Trans. Graph.*, 36(6), 2017. 2

[22] Yuki Endo, Yoshihiro Kanamori, and Jun Mitani. Deep reverse tone mapping. *ACM Trans. Graph.*, 36(6), 2017. 2

[23] Rob Fergus, Barun Singh, Aaron Hertzmann, Sam T. Roweis, and William T. Freeman. Removing camera shake from a single photograph. *ACM Trans. Graph.*, 25(3):787–794, 2006. 2

[24] Chihiro Go, Yuma Kinoshita, Sayaka Shiota, and Hitoshi Kiya. An image fusion scheme for single-shot high dynamic range imaging with spatially varying exposures. *CoRR*, abs/1908.08195, 2019. 3

[25] D. Gong, J. Yang, L. Liu, Y. Zhang, I. Reid, C. Shen, A. Van Den Hengel, and Q. Shi. From motion blur to motion flow: A deep learning solution for removing heterogeneous motion blur. In *CVPR*, pages 3806–3815, 2017. 2

[26] M. Granados, B. Ajdin, M. Wand, C. Theobalt, H. Seidel, and H. P. A. Lensch. Optimal HDR reconstruction with linear digital cameras. In *CVPR*, pages 215–222, 2010. 2, 3

[27] Yulia Gryaditskaya, Tania Pouli, Erik Reinhard, Karol Myszkowski, and Hans-Peter Seidel. Motion aware exposure bracketing for HDR video. *Comp. Graph. Forum*, 34(4):119–130, 2015. 2

[28] J. Gu, Y. Hitomi, T. Mitsunaga, and S. Nayar. Coded rolling shutter photography: Flexible space-time sampling. In *ICCP*, pages 1–8, 2010. 3

[29] S. Gu, L. Zhang, W. Zuo, and X. Feng. Weighted nuclear norm minimization with application to image denoising. In *CVPR*, pages 2862–2869, 2014. 2

[30] Shi Guo, Zifei Yan, Kai Zhang, Wangmeng Zuo, and Lei Zhang. Toward convolutional blind denoising of real photographs. In *CVPR*, 2019. 2

[31] Saghi Hajisharif, Joel Kronander, and J. Unger. HDR reconstruction for alternating gain (ISO) sensor readout. In *Eurographics*, 2014. 3

[32] Samuel W. Hasinoff, Dillon Sharlet, Ryan Geiss, Andrew Adams, Jonathan T. Barron, Florian Kainz, Jiawen Chen, and Marc Levoy. Burst photography for high dynamic range and low-light imaging on mobile cameras. *ACM Trans. Graph.*, 35(6), 2016. 2

[33] Kaiming He, Xiangyu Zhang, Shaoqing Ren, and Jian Sun. Deep residual learning for image recognition. In *CVPR*, pages 770–78, 2016. 5

[34] Glenn E Healey and Raghava Kondepudy. Radiometric ccd camera calibration and noise estimation. *IEEE PAMI*, 16(3):267–276, 1994. 2

[35] Felix Heide, Markus Steinberger, Yun-Ta Tsai, Mushfiqur Rouf, Dawid Pajak, Dikpal Reddy, Orazio Gallo, Jing Liu, Wolfgang Heidrich, Karen Egiazarian, Jan Kautz, and Kari Pulli. FlexISP: A flexible camera image processing framework. *ACM Trans. Graph.*, 33(6), 2014. 3, 6, 7

[36] Sony IMX. https://www.framos.com/en/news/sony-launches-highly-sensitive-4/3-cmos-sensor-for-4k-surveillance, accessed on Nov. 12, 2020. 1, 3

[37] James R. Janesick. *Scientific Charge-coupled Devices*. 2001. 3, 4

[38] Xixi Jia, Sanyang Liu, Xiangchu Feng, and Lei Zhang. FOC-Net: A fractional optimal control network for image denoising. In *CVPR*, 2019. 2

[39] Huaizu Jiang, Deqing Sun, Varun Jampani, Ming-Hsuan Yang, Erik Learned-Miller, and Jan Kautz. Super SloMo:

High quality estimation of multiple intermediate frames for video interpolation. In *CVPR*, 2018. 8

[40] M. Jin, Z. Hu, and P. Favaro. Learning to extract flawless slow motion from blurry videos. In *CVPR*, pages 8104–8113, 2019. 2

[41] M. Jin, G. Meishvili, and P. Favaro. Learning to extract a video sequence from a single motion-blurred image. In *CVPR*, pages 6334–6342, 2018. 2

[42] Nima Khademi Kalantari and Ravi Ramamoorthi. Deep high dynamic range imaging of dynamic scenes. *ACM Trans. Graph.*, 36(4), 2017. 2

[43] Nima Khademi Kalantari and Ravi Ramamoorthi. Deep HDR video from sequences with alternating exposures. In *Eurographics*, 2019. 2

[44] Nima Khademi Kalantari, Eli Shechtman, Connelly Barnes, Soheil Darabi, Dan B. Goldman, and Pradeep Sen. Patch-based high dynamic range video. *ACM Trans. Graph.*, 32(6), 2013. 2

[45] Sing Bing Kang, Matthew Uyttendaele, Simon Winder, and Richard Szeliski. High dynamic range video. *ACM Trans. Graph.*, 22(3):319–325, 2003. 2

[46] T. Kim and K. Lee. Generalized video deblurring for dynamic scenes. In *CVPR*, pages 5426–5434, 2015. 2

[47] T. H. Kim, K. M. Lee, B. Schölkopf, and M. Hirsch. Online video deblurring via dynamic temporal blending network. In *ICCV*, pages 4058–4067, 2017. 2

[48] J. Kronander, S. Gustavson, G. Bonnet, and J. Unger. Unified HDR reconstruction from raw CFA data. In *ICCP*, pages 1–9, 2013. 3

[49] Alexander Krull, Tim-Oliver Buchholz, and Florian Jug. Noise2void - learning denoising from single noisy images. In *CVPR*, 2019. 2

[50] Alexander Krull, Tomas Vicar, and Florian Jug. Probabilistic noise2void: Unsupervised content-aware denoising. *arXiv:1906.00651*, 2019. 2

[51] Orest Kupyn, Volodymyr Budzan, Mykola Mykhailych, Dmytro Mishkin, and Jiří Matas. Deblurgan: Blind motion deblurring using conditional adversarial networks. In *CVPR*, 2018. 2

[52] Orest Kupyn, Tetiana Martyniuk, Junru Wu, and Zhangyang Wang. Deblurgan-v2: Deblurring (orders-of-magnitude) faster and better. In *ICCV*, pages 8878–8887, 2019. 2, 5, 6

[53] Samuli Laine, Tero Karras, Jaakko Lehtinen, and Timo Aila. High-quality self-supervised deep image denoising. In *NiPS*, volume 32, pages 6970–6980, 2019. 2

[54] Stamatios Lefkimmiatis. Universal denoising networks: A novel CNN architecture for image denoising. In *CVPR*, 2018. 2

[55] Jaakko Lehtinen, Jacob Munkberg, Jon Hasselgren, Samuli Laine, Tero Karras, Miika Aittala, and Timo Aila. Noise2Noise: Learning image restoration without clean data. In *Proc. of Machine Learning Research*, volume 80, pages 2965–2974, 2018. 2

[56] Frank Lenzen and Otmar Scherzer. Partial differential equations for zooming, deinterlacing and dejittering. *Int. J Comp. Vis.*, 92:162–176, 2011. 3

[57] A. Levin, Y. Weiss, F. Durand, and W. T. Freeman. Understanding and evaluating blind deconvolution algorithms. In *CVPR*, pages 1964–1971, 2009. 2

[58] Orly Liba, Kiran Murthy, Yun-Ta Tsai, Tim Brooks, Tianfan

Xue, Nikhil Karnad, Qiurui He, Jonathan T. Barron, Dillon Sharlet, Ryan Geiss, Samuel W. Hasinoff, Yael Pritch, and Marc Levoy. Handheld mobile photography in very low light. *ACM Trans. Graph.*, 38(6), 2019. 2

[59] Ce Liu, Richard Szeliski, Sing Bing Kang, C Lawrence Zitnick, and William T Freeman. Automatic estimation and removal of noise from a single image. *IEEE PAMI*, 30(2):299–314, 2007. 2

[60] Peidong Liu, Joel Janai, Marc Pollefeys, Torsten Sattler, and Andreas Geiger. Self-supervised linear motion deblurring. *IEEE Robotics and Automation Letters*, 5(2):2475–2482, 2020. 2

[61] Ziwei Liu, Lu Yuan, Xiaoou Tang, Matt Uyttendaele, and Jian Sun. Fast burst images denoising. *ACM Trans. Graph.*, 33(6), 2014. 2

[62] Sizhuo Ma, Shantanu Gupta, Arin C. Ulku, Claudio Brushini, Edoardo Charbon, and Mohit Gupta. Quanta burst photography. *ACM Transactions on Graphics (TOG)*, 39(4), 7 2020. 2, 3

[63] S. Mann and R. W. Picard. On being 'undigital' with digital cameras: Extending dynamic range by combining differently exposed pictures. In *ISfT*, pages 442–448, 1995. 2

[64] Xiaojiao Mao, Chunhua Shen, and Yu-Bin Yang. Image restoration using very deep convolutional encoder-decoder networks with symmetric skip connections. In *NiPS*, pages 2802–2810, 2016. 1, 2

[65] D. Marnerides, T. Bashford-Rogers, J. Hatchett, and K. Debattista. Expandnet: A deep convolutional neural network for high dynamic range expansion from low dynamic range content. *Comp. Graph. Forum*, 37(2):37–49, 2018. 2

[66] T. Mertens, J. Kautz, and F. Van Reeth. Exposure fusion. In *Pacific Graphics*, pages 382–390, 2007. 2

[67] Tomer Michaeli and Michal Irani. Blind deblurring using internal patch recurrence. In *ECCV*, pages 783–798, 2014. 2

[68] B. Mildenhall, J. T. Barron, J. Chen, D. Sharlet, R. Ng, and R. Carroll. Burst denoising with kernel prediction networks. In *CVPR*, pages 2502–2510, 2018. 2

[69] T. Mitsunaga and S. K. Nayar. Radiometric self calibration. In *CVPR*, pages 374–380 Vol. 1, 1999. 2

[70] Nick Moran, Dan Schmidt, Yu Zhong, and Patrick Coady. Noisier2noise: Learning to denoise from unpaired noisy data. In *CVPR*, pages 12064–12072, 2020. 2

[71] Janne Mustaniemi, Juho Kannala, Jiri Matas, Simo Särkkä, and Janne Heikkilä. LSD$_2$-joint denoising and deblurring of short and long exposure images with convolutional neural networks. In *BMVC*, 2020. 2, 5, 6

[72] S. Nah, S. Baik, S. Hong, G. Moon, S. Son, R. Timofte, and K. M. Lee. NTIRE 2019 challenge on video deblurring and super-resolution: Dataset and study. In *CVPRW*, pages 1996–2005, 2019. 2

[73] S. Nah, T. H. Kim, and K. M. Lee. Deep multi-scale convolutional neural network for dynamic scene deblurring. In *CVPR*, pages 257–265, 2017. 1, 2

[74] Nayar and Branzoi. Adaptive dynamic range imaging: optical control of pixel exposures over space and time. In *ICCV*, pages 1168–1175 vol.2, 2003. 3

[75] S. K. Nayar, V. Branzoi, and T. E. Boult. Programmable imaging using a digital micromirror array. In *CVPR*, vol-

ume 1, pages I–I, 2004. 3

[76] Shree K. Nayar and Tomoo Mitsunaga. High dynamic range imaging: Spatially varying pixel exposures. In *CVPR*, pages 1472–1479, 2000. 3

[77] Omnivision. https://www.ovt.com/sensors/oh02a10/, accessed on Mar. 15, 2021. 5

[78] Jinshan Pan, Jiangxin Dong, Yang Liu, Jiawei Zhang, Jimmy Ren, Jinhui Tang, Yu Wing Tai, and Ming-Hsuan Yang. Physics-based generative adversarial models for image restoration and beyond. *IEEE Computer Architecture Letters*, (01):1–1, 2020. 2

[79] T. Plötz and S. Roth. Benchmarking denoising algorithms with real photographs. In *CVPR*, pages 2750–2759, 2017. 2

[80] K. R. Prabhakar, V. S. Srikar, and R. V. Babu. Deepfuse: A deep unsupervised approach for exposure fusion with extreme exposure image pairs. In *ICCV*, pages 4724–4732, 2017. 2

[81] K. Purohit, A. Shah, and A. N. Rajagopalan. Bringing alive blurred moments. In *CVPR*, pages 6823–6832, 2019. 2

[82] Yuhui Quan, Mingqin Chen, Tongyao Pang, and Hui Ji. Self2self with dropout: Learning self-supervised denoising from single image. In *CVPR*, 2020. 2

[83] Erik Reinhard, Wolfgang Heidrich, Paul Debevec, Sumanta Pattanaik, Greg Ward, and Karol Myszkowski. *High dynamic range imaging: acquisition, display, and image-based lighting*. 2010. 1

[84] Erik Reinhard, Michael Stark, Peter Shirley, and James Ferwerda. Photographic tone reproduction for digital images. *ACM Trans. Graph.*, 21(3):267–276, 2002. 5

[85] Mark A. Robertson, Sean Borman, and Robert L. Stevenson. Estimation-theoretic approach to dynamic range enhancement using multiple exposures. *J Electronic Imaging*, 12(2):219 – 228, 2003. 2

[86] Olaf Ronneberger, Philipp Fischer, and Thomas Brox. U-net: Convolutional networks for biomedical image segmentation. In *MICCAI*, pages 234–41, 2015. 5

[87] U. Schmidt, C. Rother, S. Nowozin, J. Jancsary, and S. Roth. Discriminative non-blind deblurring. In *CVPR*, pages 604–611, 2013. 2

[88] C. J. Schuler, H. C. Burger, S. Harmeling, and B. Schölkopf. A machine learning approach for non-blind image deconvolution. In *CVPR*, pages 1067–1074, 2013. 2

[89] Michael Schöberl, Alexander Belz, Arne Nowak, Jürgen Seiler, André Kaup, and Siegfried Foessel. Building a high dynamic range video sensor with spatially non-regular optical filtering. *Proc. SPIE*, 8499, 2012. 3

[90] M. Schöberl, A. Belz, J. Seiler, S. Foessel, and A. Kaup. High dynamic range video by spatially non-regular optical filtering. In *ICIP*, pages 2757–2760, 2012. 3

[91] Ulrich Seger, Uwe Apel, and Bernd Höfflinger. HDRC-imagers for natural visual perception. *Handbook of Computer Vision and Application*, 1:223–235, 1999. 2

[92] Ana Serrano, Felix Heide, Diego Gutierrez, Gordon Wetzstein, and Belen Masia. Convolutional sparse coding for high dynamic range imaging. *Comp. Graph. Forum*, 35(2), 2016. 3

[93] Wenzhe Shi, Jose Caballero, Ferenc Huszár, Johannes Totz, Andrew P Aitken, Rob Bishop, Daniel Rueckert, and Zehan Wang. Real-time single image and video super-resolution using an efficient sub-pixel convolutional neural network. In *CVPR*, pages 1874–1883, 2016. 5

[94] S. Su, M. Delbracio, J. Wang, G. Sapiro, W. Heidrich, and O. Wang. Deep video deblurring for hand-held cameras. In *CVPR*, pages 237–246, 2017. 2, 4

[95] J. Sun, Wenfei Cao, Zongben Xu, and J. Ponce. Learning a convolutional neural network for non-uniform motion blur removal. In *CVPR*, pages 769–777, 2015. 2

[96] Libin Sun, Sunghyun Cho, Jue Wang, and James Hays. Good image priors for non-blind deconvolution. In *ECCV*, pages 231–246, 2014. 2

[97] Xin Tao, Hongyun Gao, Xiaoyong Shen, Jue Wang, and Jiaya Jia. Scale-recurrent network for deep image deblurring. In *CVPR*, pages 8174–8182, 2018. 1, 2, 5, 6

[98] Michael D. Tocci, Chris Kiser, Nora Tocci, and Pradeep Sen. A versatile HDR video production system. *ACM Trans. Graph.*, 30(4), 2011. 3

[99] Dmitry Ulyanov, Andrea Vedaldi, and Victor Lempitsky. Deep image prior. In *CVPR*, 2018. 2

[100] Emergent vision. https://emergentvisiontec.com/products/area-scan-cameras/25-gige-area-scan-cameras-hb-series/hb-12000/, accessed on Mar. 15, 2021. 5

[101] Zhou Wang, Alan C Bovik, Hamid R Sheikh, and Eero P Simoncelli. Image quality assessment: from error visibility to structural similarity. *IEEE TIP*, 13(4):600–612, 2004. 6

[102] O. Whyte, J. Sivic, A. Zisserman, and J. Ponce. Non-uniform deblurring for shaken images. In *CVPR*, pages 491–498, 2010. 2

[103] P. Wieschollek, M. Hirsch, B. Schölkopf, and H. Lensch. Learning blind motion deblurring. In *ICCV*, pages 231–240, 2017. 2

[104] Shangzhe Wu, Jiarui Xu, Yu-Wing Tai, and Chi-Keung Tang. Deep high dynamic range imaging with large foreground motions. In *ECCV*, pages 120–135, 2018. 2

[105] Xiaohe Wu, Ming Liu, Yue Cao, Dongwei Ren, and Wangmeng Zuo. Unpaired learning of deep image denoising. In *ECCV*, pages 352–368. Springer, 2020. 2

[106] Jun Xu, Yuan Huang, Li Liu, Fan Zhu, Xingsong Hou, and Ling Shao. Noisy-as-clean: Learning unsupervised denoising from the corrupted image. *arXiv preprint arXiv:1906.06878*, 2019. 2

[107] Li Xu and Jiaya Jia. Two-phase kernel estimation for robust motion deblurring. In *ECCV 2010*, pages 157–170, 2010. 2

[108] Li Xu, Jimmy SJ Ren, Ce Liu, and Jiaya Jia. Deep convolutional neural network for image deconvolution. In *NiPS*, pages 1790–1798, 2014. 2

[109] Lu Yuan, Jian Sun, Long Quan, and Heung-Yeung Shum. Image deblurring with blurred/noisy image pairs. *ACM Trans. Graph.*, 26(3):1–es, 2007. 2

[110] Kai Zhang, Wangmeng Zuo, Yunjin Chen, Deyu Meng, and Lei Zhang. Beyond a gaussian denoiser: Residual learning of deep CNN for image denoising. *IEEE TIP*, 26(7):3142–3155, 2017. 2

[111] Kai Zhang, Wangmeng Zuo, and Lei Zhang. FFDNet: Toward a fast and flexible solution for CNN-based image denoising. *IEEE TIP*, 27(9):4608–4622, 2018. 1, 2, 5, 6

[112] Xinyi Zhang, Hang Dong, Zhe Hu, Wei Sheng Lai, Fei Wang, and Ming Hsuan Yang. Gated fusion network for joint image deblurring and super-resolution. In *BMVC*, 2019. 2

[113] Yulun Zhang, Kunpeng Li, Kai Li, Lichen Wang, Bineng Zhong, and Yun Fu. Image super-resolution using very deep

residual channel attention networks. *CoRR*, abs/1807.02758, 2018. 8

[114] Hang Zhao, Orazio Gallo, Iuri Frosio, and Jan Kautz. Loss functions for image restoration with neural networks. *IEEE TIP*, 3(1):47–57, 2016. 5

[115] Zhihang Zhong, Gao Ye, Yinqiang Zheng, and Zheng Bo. Efficient spatio-temporal recurrent neural network for video deblurring. In *ECCV*, 2020. 2

[116] Shangchen Zhou, Jiawei Zhang, Jinshan Pan, Haozhe Xie, Wangmeng Zuo, and Jimmy Ren. Spatio-temporal filter adaptive network for video deblurring. In *ICCV*, 2019. 2

[117] Jun-Yan Zhu, Taesung Park, Phillip Isola, and Alexei A Efros. Unpaired image-to-image translation using cycle-consistent adversarial networks. In *ICCV*, pages 2223–32, 2017. 2

[118] D. Zoran and Y. Weiss. From learning models of natural image patches to whole image restoration. In *ICCV*, pages 479–486, 2011. 2

[119] U. Çoğalan and A. O. Akyüz. Deep joint deinterlacing and denoising for single shot dual-ISO HDR reconstruction. *IEEE TIP*, 29:7511–7524, 2020. 3